X-ray phase contrast imaging with kilometer propagation distance within a meter

Rebecca Spiecker *
Laboratory for Applications of Synchrotron Radiation, Karlsruhe Institute of Technology, 76131 Karlsruhe, Germany and Institute for Photon Science and Synchrotron Radiation, Karlsruhe Institute of Technology, 76344 Eggenstein-Leopoldshafen, Germany

Martin Spiecker
Laboratory for Applications of Synchrotron Radiation, Karlsruhe Institute of Technology, 76131 Karlsruhe, Germany; Institute for Quantum Materials and Technologies, Karlsruhe Institute of Technology, 76344 Eggenstein-Leopoldshafen, Germany; and Physikalisches Institut, Karlsruhe Institute of Technology, 76131 Karlsruhe, Germany

Adyasha Biswal
Laboratory for Applications of Synchrotron Radiation, Karlsruhe Institute of Technology, 76131 Karlsruhe, Germany; Institute for Photon Science and Synchrotron Radiation, Karlsruhe Institute of Technology, 76344 Eggenstein-Leopoldshafen, Germany; and Centre for Organismal Studies, Heidelberg University, 69120 Heidelberg, Germany

Mykola Shcherbinin
Laboratory for Applications of Synchrotron Radiation, Karlsruhe Institute of Technology, 76131 Karlsruhe, Germany

Tilo Baumbach
Laboratory for Applications of Synchrotron Radiation, Karlsruhe Institute of Technology, 76131 Karlsruhe, Germany and Institute for Photon Science and Synchrotron Radiation, Karlsruhe Institute of Technology, 76344 Eggenstein-Leopoldshafen, Germany

(Received 28 October 2023; revised 29 March 2024; accepted 4 November 2025; published 19 December 2025)

We introduce an x-ray imaging technique to facilitate dose-efficient propagation-based phase contrast imaging (PB-PCI) of large, centimeter-sized samples. The dose efficiency is realized by generating image contrast for low sampling frequencies, i.e., large pixel sizes, which would require propagation distances of tens to hundreds of meters in conventional PB-PCI. By magnifying the spatial frequency distribution of the diffracted wave field behind the sample, we strongly enhance the image contrast at short physical propagation distances, corresponding to kilometer-long distances. For this purpose, the wave field is demagnified by asymmetric Bragg crystal optics. Concomitantly, the crystal arrangement substantially reduces image blur caused by the finite x-ray source size. We demonstrate experimentally the significant increase in image contrast compared to conventional PB-PCI at the same short physical propagation distance. In combination with a subsequent Bragg magnifier, the method will allow for an even higher dose efficiency, rendering this technique a potential candidate for, e.g., low-dose (bio)medical diagnostics.

DOI: 10.1103/pkmv-x47f

I. INTRODUCTION

Conventional x-ray imaging relies on the attenuation of x-rays in a medium and is well suited for highly absorbing materials, but yields only vanishingly low contrast for soft materials and tissues [1]. Phase contrast imaging can overcome these limitations by uncovering the phase shift that the sample imprints on the x-ray wave field [1,2]. In the last decades, multiple phase contrast imaging techniques have been developed [2–7], finding application in various fields such as materials science [8], natural and cultural heritage [9], biology [10,11], and industrial and medical applications [12–16].

For phase contrast imaging of large, centimeter-sized samples, it is essential to attain contrast for low sampling frequencies, in particular for flux-limited applications such as low-dose or fast imaging, where a compromise has to be taken between deposited dose or exposure time on the one hand and spatial resolution on the other hand. Currently, the main approaches for phase contrast imaging of large samples at moderate resolution above $\sim$10 µm use differential phase contrast, e.g., analyzer- [17,18], grating- [4,19,20], or speckle-based imaging [21,22]. A further and complementary approach is propagation-based phase contrast imaging (PB-PCI) [23–30]. PB-PCI utilizes the coherent self-interference of the transmitted wave field behind the sample, which gradually evolves into intensity contrast

*Contact author: rebecca.spiecker@kit.edu

Published by the American Physical Society under the terms of the Creative Commons Attribution 4.0 International license. Further distribution of this work must maintain attribution to the author(s) and the published article's title, journal citation, and DOI.

with increasing propagation distance. However, to visualize low spatial frequencies of $\sim 2\pi/10\,\mu\text{m}$ to $\sim 2\pi/1\,\text{mm}$, long propagation distances are necessary [26–38], ideally tens to hundreds of meters. Recently, a beamline has been built at the European Synchrotron Radiation Facility (ESRF, Grenoble, France) with a remarkably long experimental hutch of 45 m, which facilitates PB-PCI at propagation distances of up to 36 m, tailored to the x-ray source size [35,39,40].

Here, we describe an approach that enables PB-PCI at moderate resolution with a physical distance between sample and detector in the submeter range, yet allowing for long effective propagation distances of hundreds to thousands of meters. For this purpose, the spatial frequency distribution of the diffracted x-ray wave field behind the sample is magnified by asymmetric Bragg diffraction, resulting in strongly increased effective propagation distances. We show experimentally that the proposed method leads to a significantly enhanced image contrast, which would not be achievable by conventional PB-PCI, even at such long physical propagation distances, due to the finite size of the X-ray source. In the following, we outline the basic working principle, describe the realization by Bragg crystal optics, and show a first proof-of-concept experiment.

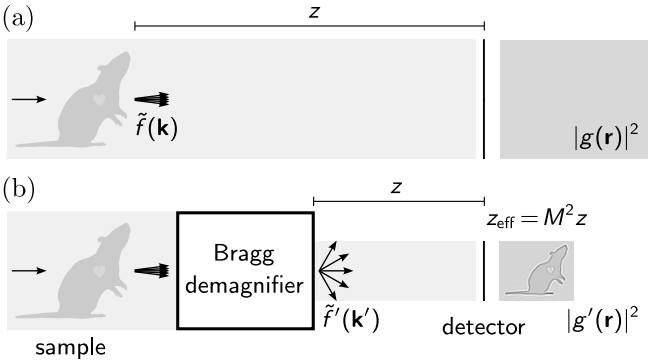


FIG. 1. Working principle of the Bragg demagnifier for PB-PCI at low spatial frequencies, illustrated for a pure phase object. (a) When imaging with conventional PB-PCI at moderate resolution, short physical propagation distances z do not yield sufficient image contrast in the detected image $|g(\mathbf{r})|^2$. (b) Broadening the spatial frequency distribution $\tilde{f}(\mathbf{k})$ of the diffracted wave field behind the sample by a factor M, i.e., $\mathbf{k}' = M \cdot \mathbf{k}$, leads to significantly higher image contrast within a short physical propagation distance z. The contrast obtained in the image $|g'(\mathbf{r})|^2$ corresponds to an effective propagation distance $z_{\text{eff}} = M^2 z$.

II. RESULTS AND DISCUSSION

A. Working principle

The working principle can be explained in the frame of the Fresnel diffraction theory and assuming monochromatic plane wave illumination of the sample. The complex-valued wave field $f(\mathbf{r})$ in the sample exit plane at $z = 0$ can be represented by its Fourier transform $\tilde{f}(\mathbf{k})$, where $\mathbf{r} = (x, y)^{\text{T}}$ and $\mathbf{k} = (k_x, k_y)^{\text{T}}$ denote the spatial coordinate and angular spatial frequency, respectively. After free space propagation along a distance z, the wavefield $g(\mathbf{r})$ in the image plane is given by

$$g(\mathbf{r}) = \frac{1}{2\pi} \iint \tilde{f}(\mathbf{k}) e^{-i\frac{\mathbf{k}^2}{2k_0}z} e^{i\mathbf{k}\mathbf{r}} \mathrm{d}k_x \mathrm{d}k_y, \tag{1}$$

where k_0 is the angular wave number in vacuum and $e^{-i\frac{\mathbf{k}^2}{2k_0}z}$ is denoted as the Fresnel propagator [41]. The argument $\frac{\mathbf{k}^2}{2k_0}z$ shows that low spatial frequencies in the wave field need a long propagation distance to accumulate a certain phase shift, which can be converted into measurable intensity contrast. For imaging large samples at moderate resolution, it would thus be desirable to magnify the spatial frequencies of the sample exit wave field in order to avoid physical propagation distances of tens to hundreds of meters (see Fig. 1). By magnifying the spatial frequencies by a factor M, the transformed wave field $\tilde{f}'$ is given by $\tilde{f}'(\mathbf{k}') = \tilde{f}(\mathbf{k}'/M)$. Substitution of $\mathbf{k} = \mathbf{k}'/M$ yields the wave field

$$g'(\mathbf{r}) = \frac{M^2}{2\pi} \iint \tilde{f}(\mathbf{k}) e^{-i\frac{\mathbf{k}^2}{2k_0}M^2 z} e^{i\mathbf{k}M\mathbf{r}} \mathrm{d}k_x \mathrm{d}k_y \tag{2}$$

in the image plane after propagation of the modified wave field along the physical distance z. The expansion of the frequency spectrum thus leads to an enhanced effective propagation distance $z_{\text{eff}} = M^2 z$ that is quadratic in M. The image acquired at the physical distance z will therefore exhibit the same contrast as the unaltered wave field after the propagation distance $M^2 z$. By the term $M\mathbf{r}$ in Eq. (2) we recognize that the magnification of the spatial frequencies comes along with a demagnification in real space. The demagnified and propagated image can be either detected by a high-resolution detector, which, however, has a limited detection efficiency, or subsequently remagnified for being detected with an efficient large-area detector [42] (see also Appendixes). For a resolution of a few lp/mm as can be found in medical x-ray imaging [43], we deduce a gain in dose efficiency of about two orders of magnitude for the proposed method compared to conventional PB-PCI at the currently longest available physical propagation distance of 36 m. For an illustrative simulation example, see Appendixes.

Demagnifying the x-ray wave field with minimal distortion can be achieved by using a so-called Bragg magnifier with reversed optical path (see Fig. 2, right). A Bragg magnifier magnifies an x-ray wave field by asymmetric Bragg diffraction [42,44–50]. In this case, the asymmetry angle α between the crystal surface and the reflecting lattice planes is defined as positive. In contrast, the wave field is compressed when the asymmetry angle is negative. So far, demagnification by asymmetric Bragg diffraction has been employed for focusing the incident x-ray illumination [50–52], to achieve a high angular sensitivity in analyzer-based imaging [17] or to fit a large x-ray image onto a smaller detector [53]. Here, we use demagnification to specifically increase the image contrast in PB-PCI. In our case, the Bragg demagnifier consists of two crystals for demagnification in x and y directions, respectively. The centers of the crystal reflectivity curves are aligned to the optical axis. The dependency between the spatial frequencies k_{in} and k_{out} of the wave field in front of and behind the crystals is in general a slightly nonlinear function (see Appendixes), causing the image formation to be shift variant. To keep the following discussion simple, we can assume in good approximation $k_{\text{out}}(k_{\text{in}}) \approx M k_{\text{in}}$, restoring the shift invariance. The

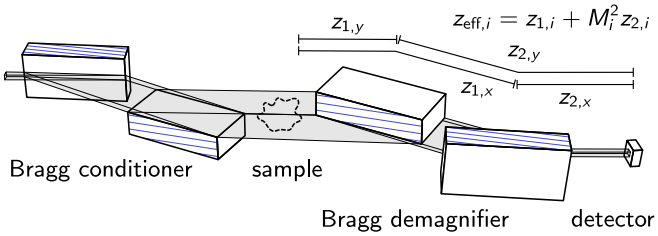


FIG. 2. Schematic of the crystal arrangement. The first two crystals magnify the incoming x-ray beam cross section in horizontal and vertical directions. The diffracted wave field behind the sample propagates along the distances $z_{1,i}$ and is then demagnified in vertical and horizontal directions by factors M_i. After free space propagation of the demagnified wave field by the distances $z_{2,i}$, we record the image with a high-resolution scintillator-based detector. Alternatively, the x-ray wave field may again be magnified to be recorded efficiently, e.g., with a single-photon counting detector [42]. The demagnification in real space leads to a magnification of the spatial frequency distribution, thereby strongly increasing the effective propagation distances $z_{\mathrm{eff},i}$. The blue lines illustrate the crystal lattice planes.

demagnification factor M is given by [45]

$$M = \frac{\sin(\theta_\mathrm{B} + \Delta\theta_\mathrm{oc} - \alpha)}{\sin(\theta_\mathrm{B} + \Delta\theta_\mathrm{hc} + \alpha)}.$$

Here, $\alpha < 0$ is the asymmetry angle, θ_B the Bragg angle, and $\Delta\theta_\mathrm{oc}$ and $\Delta\theta_\mathrm{hc}$ are refraction correcting terms from dynamical diffraction theory for the incident and outgoing wave fields, respectively [54].

Since the two crystals cannot be physically positioned at the same location, the horizontal and vertical compression of the wave field occurs at different distances $z_{1,x}$ and $z_{1,y}$ along the optical axis between the sample and crystal centers. Likewise, the distances $z_{2,x}$ and $z_{2,y}$ between the crystal centers and the detector are different as well. The demagnified wave field in the detector plane is given by

$$g'(\mathbf{r}) = \frac{M_x M_y}{2\pi} \iint \tilde{f}(\mathbf{k}) H(\mathbf{k})\, e^{ik_x M_x x} e^{ik_y M_y y} \mathrm{d}k_x \mathrm{d}k_y, \qquad (3)$$

with the propagator

$$H(\mathbf{k}) = R(\mathbf{k}) e^{-i\frac{k_x^2}{2k_0}\left(z_{1,x} + M_x^2 z_{2,x}\right)} e^{-i\frac{k_y^2}{2k_0}\left(z_{1,y} + M_y^2 z_{2,y}\right)}. \qquad (4)$$

In $R(\mathbf{k})$, we have combined the complex crystal reflection of the diffracted wave field amplitudes of both crystals [54]. M_x and M_y are the demagnification factors in horizontal and vertical directions, respectively. The different distances and potentially different demagnifications lead to different effective propagation distances

$$z_{\mathrm{eff},i} = z_{1,i} + M_i^2 z_{2,i}$$

in horizontal and vertical directions. For large M, the propagation along $z_{1,i}$ in front of the demagnifier crystals, i.e., before demagnification, can be neglected. At third-generation synchrotrons, vertical demagnification is therefore ideally performed first, since the source size is smaller in vertical direction than horizontally, allowing for longer propagation distances before the onset of source blur. Finally, the highest resolvable spatial frequency k_max is restricted by the angular acceptance ω_oc of the crystals, also denoted as the input Darwin width [54]. In accordance with Abbe's criterion, it holds $k_\mathrm{max} = k_0 \omega_\mathrm{oc}/2$ [55].

A prerequisite for imaging with a Bragg demagnifier is a monochromatic x-ray beam with sufficient transversal coherence and a large beam cross section to illuminate the sample. In combination with a double-crystal monochromator, synchrotron beamlines of third and fourth generations provide low divergence and high monochromaticity. However, they usually offer only a limited, millimeter-sized beam cross section and finite transversal coherence at the sample position [56–58]. Here, we magnify the beam cross section in front of the sample by a Bragg magnifier, which we denote as Bragg conditioner (see Fig. 2, left) [59–61]. In addition, this Bragg conditioner further increases the transversal coherence and reduces the monochromatic beam divergence to well below the incident angular acceptance of the demagnifier. Besides, such a Bragg conditioner has the ability to counteract energy dispersion effects of the Bragg demagnifier, as we will revisit later.

B. Experimental realization and discussion

As a proof of concept, we realize a Bragg demagnifier for an energy range 29–31 keV. A schematic of the crystal arrangement is given in Fig. 2. The incident x-ray beam is expanded in two dimensions by a Bragg conditioner, traverses the sample, is demagnified by the Bragg demagnifier, and propagates to the detector plane. Here, we operate the system at 29 keV, where the demagnification factor of the crystals is $M = 25.7$, resulting in effective propagation distances of $z_{\mathrm{eff},x} \approx 380$ m and $z_{\mathrm{eff},y} \approx 600$ m. The nominal resolution limit as introduced above is 68 µm for the chosen settings. Since the image is demagnified, we detect the x-ray image using a high-resolution scintillator-based indirect detector (67 ms exposure time). The effective pixel size in the object amounts to 37 µm. For comparison to conventional free space propagation at the same physical distance, we acquire images without the demagnifier and using a large-area detector of similar pixel size (49 µm), placed at 1 m from the sample. To resolve the slight absorption contrast with the conventional setup, a statistics of ∼15 000 detected x-ray photons per pixel was used for both setups. For details on the experimental setup and parameters, see Appendixes.

In Fig. 3, we display example images (after flat- and dark-field correction) of a blackberry leaf, a mouse liver lobe in an ethanol bag, and a salamander in a tube filled with ethanol. For conventional PB-PCI, the leaf exhibits only very weak contrast caused by absorption in the sample, as shown in the inset, while the leaf veins are well visible with the demagnifier. The liver is not discernible at all in the conventional image. In contrast, the demagnifier brings to light a net of blood vessels due to the strongly increased propagation distance. A similar contrast enhancement is observed for the salamander: In the conventional PB-PCI image, only the bones and otoliths are weakly visible, while the demagnifier reveals the internal structures.

The images acquired with the Bragg demagnifier certainly show patterns that are brighter than the background, indicating constructive interference generated by PB-PCI. However, at

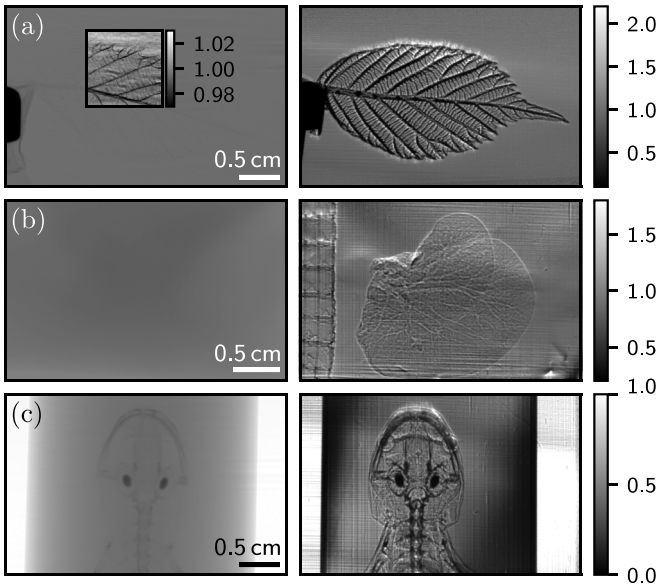


FIG. 3. Comparison of PB-PCI of low spatial frequencies using conventional free space propagation (left) and the Bragg demagnifier (right). In both setups, the incident x-ray beam was expanded in front of the sample by a Bragg conditioner [62] and the physical propagation distance was ∼1 m. For the Bragg demagnifier, this corresponds to effective propagation distances of $z_{\mathrm{eff},x} \approx 380\,\mathrm{m}$ and $z_{\mathrm{eff},y} \approx 600\,\mathrm{m}$, achieved by a demagnification of $M = 25.7$. (a) Blackberry leaf in air. With conventional PB-PCI, only marginal absorption contrast can be seen, as shown in the inset with adjusted gray scale. The Bragg demagnifier provides strong propagation-based phase contrast. (b) Mouse liver lobe in ethanol. Conventional PB-PCI does not reveal any contrast, whereas the Bragg demagnifier brings to light a net of blood vessels. The tape left to the sample becomes visible as well. (c) Salamander in ethanol. The Bragg demagnifier yields strong image contrast and allows to visualize soft tissues, while conventional PB-PCI yields only little absorption and no phase contrast. The colorbar indicates the intensity values of the flat- and dark-field corrected images.

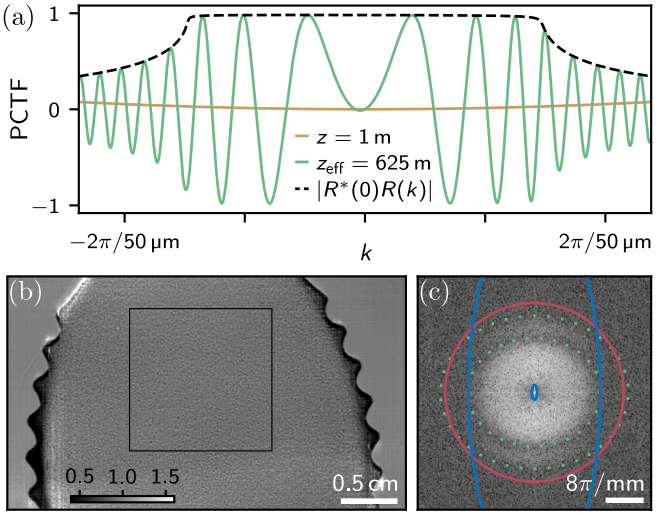


FIG. 4. (a) PCTF [see Eq. (5)] of weak phase objects over spatial frequencies k for conventional PB-PCI (brown) and using the Bragg demagnifier (green, black envelope) with a demagnification of $M = 25$. (b) Plastic spoon imaged with the Bragg demagnifier and (c) Fourier spectrum of the area marked in panel (b), plotted as $\log(|\tilde{I}(\mathbf{k})|)$. The spoon's rough surface acts as a weak phase noise object. The elliptic Thon rings originate from the roots of the PCTF with $z_{\mathrm{eff},x} \approx 380\,\mathrm{m}$ and $z_{\mathrm{eff},y} \approx 600\,\mathrm{m}$. The first two zero crossings are indicated in green. Contrast degradation to $1/e$ due to the finite source size is shown by the outer blue line. Expected contrast degradation at hypothetical physical propagation distances of $z_i = z_{\mathrm{eff},i}$ for conventional PB-PCI is indicated by the inner blue line. The red circle shows the $1/e$ contrast degradation by the optical microscope.

the edges of the crystals where the background intensity is reduced, we observe also other bright patterns after flat-field correction, e.g., at the upper edge of the leaf and at the mouth of the salamander. These artifacts arise most likely from the curvature of the incident wave field, which, at the crystal edges, deviates from the center of the crystal reflectivity curve, thereby generating diffraction-enhanced contrast [18]. In a future setup, the curvature may be reduced by collimating the x-ray beam in front of the Bragg conditioner by compound refractive lenses [63]. Furthermore, the presented images partially contain extinction contrast as known from analyzer-based imaging [64], which occurs when x-rays are scattered to angles higher than the crystal's angular acceptance and are thus not transferred into the image. We attribute, for example, the dark spots in the salamander, the otoliths, not only to absorption but also to extinction contrast, since their intensity is reduced with the demagnifier. Extinction contrast is also observed in the bones. Note that even though the angular acceptance of the demagnifier crystals is small and therefore sensitive for extinction contrast, there is no average intensity decrease in the soft tissue regions of the samples shown in Fig. 3. This implies that valuable information is encoded in low spatial frequencies within the angular acceptance, which are now made visible by the Bragg demagnifier through the enhanced PB-PCI.

To prove the presence of interference resulting from the increased effective propagation distance, we imaged a plastic spoon with a rough surface, which acts as a weak phase noise object. For weak phase objects, the contrast formation $I(\mathbf{r}) = |g'(\mathbf{r})|^2$ reduces to a linear process, and the image intensity in Fourier space is given by $\tilde{I}(\mathbf{k}) \approx \delta(\mathbf{k}) - 2\mathrm{Im}[H^*(\mathbf{0})H(\mathbf{k})]\tilde{\varphi}(\mathbf{k})$ [65,66]. Here, $\tilde{\varphi}(\mathbf{k})$ denotes the phase shift in Fourier space of the sample exit wave field. The absorption μ enters similarly via the real part but is omitted here for clarity. Insertion of the propagator yields

$$\tilde{I}(\mathbf{k}) \approx \delta(\mathbf{k}) + 2|R^*(\mathbf{0})R(\mathbf{k})| \sin\left(\frac{\mathbf{k}^2 \mathbf{z}_{\mathrm{eff}}}{2k_0} + \phi_R\right)\tilde{\varphi}(\mathbf{k}), \quad (5)$$

where ϕ_R is a slowly varying correction from the complex crystal reflectivity. The conversion of phase information into image intensity defines the so-called phase contrast transfer function (PCTF). Analogously, replacing the sine by a cosine yields the amplitude contrast transfer function, which, however, only plays a minor role since μ is typically several orders of magnitude smaller than φ [67]. As a side note, Eq. (5) emphasizes the need for long propagation distances for imaging low spatial frequencies. As an example, Fig. 4(a) shows the free space PCTF for $z = 1\,\mathrm{m}$ (brown). It generates almost no contrast. In contrast, a Bragg demagnifier with a

demagnification factor of $M = 25$ and a physical distance between crystal and detector of only 1 m exhibits high values in the PCTF (green). The PCTF corresponds to conventional free space propagation with a distance of $z = 625$ m, overlaid by the field amplitude reflection of the crystals (black). In the Fourier spectrum of the plastic spoon, so-called Thon rings become visible [Figs. 4(b) and 4(c)] [68]. They correspond to spatial frequencies where the PCTF is close to zero and are an additional evidence for the presence of interference. From the position of the Thon rings, the defocus and astigmatism can be extracted [69], as commonly done in electron microscopy [70,71]. We extract propagation distances of $z_{\mathrm{eff},x} \approx 380$ m and $z_{\mathrm{eff},y} \approx 600$ m, in correspondence with the experimental settings.

Next, we consider the effect of source blur on the image degradation. The monochromator delivers an energy distribution and a corresponding angular distribution given by the size of the polychromatic source. The virtual source size is typically increased when the x-rays pass through asymmetric crystals [72]. For our conditioner, we calculate a virtual spread by a factor of ~ 3. Using the same pair of crystals for the conditioner and demagnifier, the increase of the virtual source size can exactly be compensated [72]. This means that the demagnified image experiences the source blur of its physical propagation distance z. Since the image was demagnified by a factor of M, the source blur is a factor of M better compared to the image blur at a physical propagation distance of $M^2 z$. This effect is demonstrated in Fig. 4(c). Assuming a Gaussian distribution for the source function, standard deviations of $\sigma_x = 164$ µm and $\sigma_y = 38$ µm in horizontal and vertical directions, respectively, have been extracted for the P23 source in preceding measurements [73]. The resulting contrast degradation to $1/e$ at the physical propagation distances is depicted by the outer blue line. A hypothetical physical propagation distance of $z_i = z_{\mathrm{eff},i}$ without demagnifier would suppress most of the image information, as shown by the inner blue line. For completeness, we also indicate the $1/e$ degradation by the optical transfer function of the indirect detector system (see Ref. [42]). The formation of additional Thon rings in vertical direction may further be suppressed since the spoon does not deliver a white noise power spectrum.

Instead of detecting the demagnified image with a high-resolution detector, the wave field can also be remagnified with a Bragg magnifier and detected by a highly efficient large-area detector [42]. The contrast enhancement achieved with the demagnifier, in conjunction with a subsequent magnifier and large-area detector, would allow imaging the samples shown in Fig. 3 with a drastically reduced x-ray fluence of, e.g., $\sim$100 ph/px, as was used in the *in vivo* wasp video in Ref. [42] for micrometer resolution. In this way, the technique would enable fast (<1 ms) *in vivo* imaging with highest dose efficiency at moderate resolution. Moreover, the shift variance is exactly compensated by the additional magnifier when employing the same crystals as for the demagnifier (see Appendixes), allowing the image formation to be efficiently modeled in Fourier space. In future, the mechanical stability of the crystals has to be further improved, which would also allow for tomography and employment of larger crystals and higher energies as well as a stable combination of a Bragg conditioner, demagnifier, and magnifier.

III. CONCLUSION

We have presented an imaging technique to facilitate propagation-based x-ray phase contrast imaging of low spatial frequencies to image large, centimeter-sized samples in a dose-efficient manner at moderate resolution and in a compact meter-scale setup. For illuminating the sample, a Bragg conditioner is used in front of the sample to enlarge the beam cross section of the millimeter-sized synchrotron beam, thereby also increasing the monochromatic transversal coherence. By demagnifying the x-ray wave field behind the sample with a Bragg demagnifier, the effective propagation distance is strongly increased. In this way, the image contrast is significantly enhanced compared to conventional phase contrast imaging at the same physical propagation distance, as we verified experimentally. Simultaneously, image blur by the finite source size is reduced. By magnifying the propagated wave field with a Bragg magnifier onto an efficient large-area detector, the technique may find utility for dose-efficient applications, e.g., in medical diagnostics in conjunction with compact x-ray sources [74–77] for the early detection of breast cancer or other diseases.

ACKNOWLEDGMENTS

We acknowledge DESY (Hamburg, Germany), a member of the Helmholtz Association HGF, for the provision of experimental facilities. Experiments were carried out at P23, PETRA III, in the frame of the KIT-DESY "Hierarchical Imaging Karlsruhe" collaboration, and we would like to thank Carlos Sato Baraldi Dias, Mateusz Czyzycki, and Dmitri Novikov for assistance at the beamline. We are grateful to Simon Merz, Lea Bornemann (both Miltenyi Biotec), and Quentin Martinez (Stuttgart State Museum of Natural History) for providing the mouse liver lobe and salamander specimen, respectively. Further, we thank Stefan Uhlemann and Tobias Hilvering for technical assistance and Stephen Doyle for language revision. The research was funded by the German Federal Ministry of Education and Research via Grant No. 05K2019 (HIGH-LIFE).

DATA AVAILABILITY

The data that support the findings of this article are not publicly available. The data are available from the authors upon reasonable request.

APPENDIX A: IMAGE SIMULATIONS

As an illustrative example of the benefits of the proposed method compared to conventional PB-PCI, numerical image simulations have been performed for the object shown in Fig. 5(a) with a pixel size of 50 µm. A maximum phase shift of 1 rad was chosen, corresponding to 2.5 mm thick soft tissue ($H_{54}C_5N_1O_{26}$, density of 1 g/cm^3) in water at an x-ray photon energy of 30 keV. In Fig. 5(a), we show only the phase shift of the object function. The attenuation difference is proportional to the phase shift and reaches a maximum value of 0.3%. Figures 5(b) and 5(d) show the simulated image intensity for conventional PB-PCI at physical propagation distances of $z = 36$ m and $z = 660$ m with $E = 30$ keV, and Figs. 5(c) and 5(e)

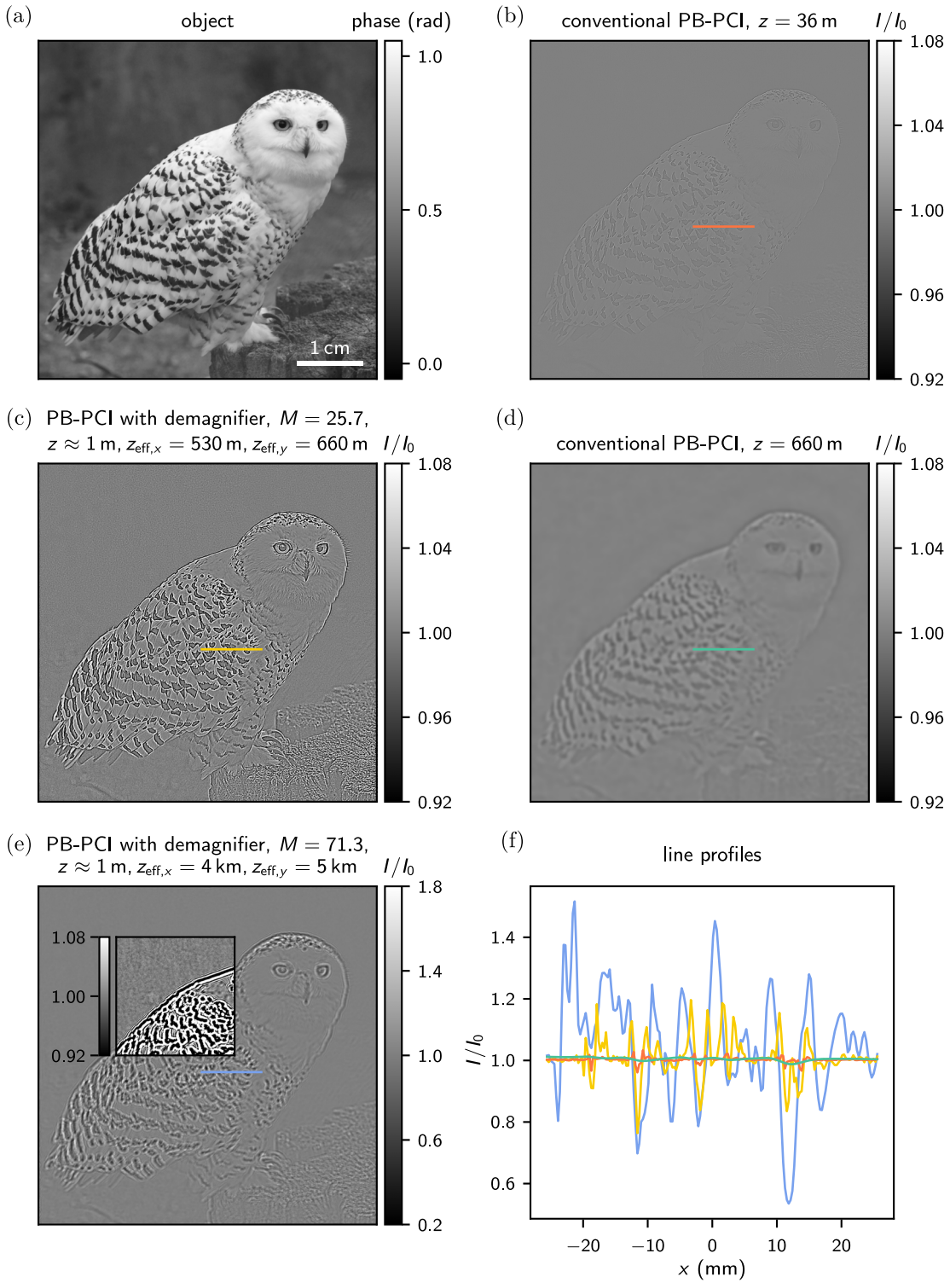


FIG. 5. Image simulations for conventional PB-PCI and using the Bragg demagnifier. (a) Phase of the object wave field. (b), (d) Conventional PB-PCI at a physical propagation distance of $z = 36$ m, which has been realized at BM18 [35,39,40], and a hypothetical physical propagation distance of $z = 660$ m, respectively. (c), (e) PB-PCI with the Bragg demagnifier, $M = 25.7$ or $M = 71.3$, respectively, and physical distances of $z_x = 0.8$ m, $z_y = 1$ m after demagnification. These parameters result in effective propagation distances of $z_{\mathrm{eff},x} = 530$ m, $z_{\mathrm{eff},y} = 660$ m or $z_{\mathrm{eff},x} = 4$ km, $z_{\mathrm{eff},y} = 5$ km, respectively. Note the difference in the color scale by a factor of 10 in panel (e). The simulations have been performed with source blur, corresponding to the vertical source size measured at P23, PETRA III [73]. For more details, see text. (f) Intensity line profiles as marked in panels (b)–(e). Note, to allow for a better comparison, the images have been normalized to the average image intensity.

depict the image intensity using the Bragg demagnifier with a demagnification of $M = 25.7$ ($E = 29\,\mathrm{keV}$) and $M = 71.3$ ($E = 30.5\,\mathrm{keV}$) and physical distances of $z_x = 0.8\,\mathrm{m}$, $z_y = 1.0\,\mathrm{m}$, corresponding to effective propagation distances of $z_{\mathrm{eff},x} = 530\,\mathrm{m}$, $z_{\mathrm{eff},y} = 660\,\mathrm{m}$ or $z_{\mathrm{eff},x} = 4\,\mathrm{km}$, $z_{\mathrm{eff},y} = 5\,\mathrm{km}$, respectively. Conventional PB-PCI has been simulated using Eq. (1). For the simulations with the Bragg demagnifier, Eq. (3) has been used, which, besides the free space propagation, also takes into account the demagnification of the wave field and the influence of the complex crystal reflectivity curve. All simulations have been performed including source blur, with a source-to-sample distance of 86 m and a source size of $\sigma = 38\,\mu\mathrm{m}$ [i.e., 90 µm full width at half maximum (FWHM)]. The latter value has been measured for the vertical source size of the P23 beamline at PETRA III [73], and was used here for both the horizontal and vertical source sizes, thereby simulating an achievable contrast at P23 toward the perspective fourth-generation synchrotron radiation facility PETRA IV [78]. For more details, see Ref. [73].

While conventional PB-PCI at 36 m yields only low contrast [Fig. 5(b)], the contrast is significantly increased for the demagnifier with an effective propagation distance of $z_{\mathrm{eff}} = 660\,\mathrm{m}$ [Fig. 5(c)]. For a hypothetical physical propagation distance of 660 m in conventional PB-PCI, source blur strongly impairs the image quality and resolution [Fig. 5(d)], which is not the case for the demagnifier, since the source size is effectively reduced by a factor M. Further increasing M and thereby z_{eff} leads to even stronger image contrast [Fig. 5(e)]. For the source parameters of P23, conventional PB-PCI at 5 km would not yield any contrast at all due to source blur, and is therefore not shown here. The contrast enhancement obtained by the demagnifier also becomes apparent in the line profiles shown in Fig. 5(f).

An appropriate measure for the increase in dose efficiency is the mean squared deviation of the image intensity distribution [42]. In comparison to the longest currently available physical propagation distance of 36 m [35,39,40] at the above-mentioned source parameters of P23 and for this example object, we extract a loss in dose efficiency of 0.3 for conventional PB-PCI at 660 m (due to source blur), but a gain in dose efficiency of 62 and 258 for the Bragg demagnifier with $M = 25.7$ ($z_{\mathrm{eff}} = 660\,\mathrm{m}$) and $M = 71.3$ ($z_{\mathrm{eff}} = 5\,\mathrm{km}$), respectively. Compared to a physical propagation distance of 10 m (not shown in Fig. 5), which is realized, e.g., at ID17 at the ESRF [29,33] or at the Imaging and Medical Beamline (IMBL) of the Australian Synchrotron [34], the extracted gain in dose efficiency is a factor of 2 for conventional PB-PCI at 660 m, and a factor of 361 and 1550 for the Bragg demagnifier with $M = 25.7$ and $M = 71.3$.

To illustrate the effects of the source size, image simulations of the same object have also been performed for the source properties of the BM18 beamline at the ESRF-EBS storage ring as given in the literature (175 m source-to-sample distance, 6.4 µm × 26 µm FWHM source size, which relates to the standard deviation σ of the Gaussian source function as $\mathrm{FWHM} = 2.355\sigma$) [40]. BM18 is the state-of-the-art beamline for PB-PCI at the addressed resolution regime. The results are depicted in Fig. 6. Compared to the obtained image at 36 m physical propagation distance [not shown here since it is similar to Fig. 5(b)], the extracted gain in dose efficiency for these BM18 source parameters is a factor of 42 and 173 for the Bragg demagnifier with $M = 25.7$ [Fig. 6(a)] and $M = 71.3$ [Fig. 6(c)], respectively, which is achieved within a meter-scale setup. For conventional PB-PCI at 660 m [Fig. 6(b)] and 5 km [Fig. 6(d)], the extracted gain is a factor of 30 and 38. Thus, in principle, a source with such good properties would enable a substantial gain by conventional PB-PCI when constructing such long beamlines of up to about 1 km [Fig. 6(b)]. Our proposed method is a very compact alternative for achieving similar image contrast, i.e., dose efficiency, and would enable even longer effective propagation distances [Fig. 6(c)] and thus higher image contrast before the onset of source blur. These simulations underline the benefits of the Bragg demagnifier approach, also for fourth-generation synchrotron sources.

TABLE I. Calculated parameters for the Si (220) Bragg demagnifier with an asymmetry angle of $\alpha = -5.92^\circ$. The intrinsic resolution limit $\lambda_{\mathrm{min}} = 2\pi/k_{\mathrm{max}}$, the demagnification factor M, and the gain factor M^2 in propagation distance are given for several energies E.

E (keV)	λ_{min} (µm)	M	M^2
29.0	68	25.7	660
30.0	91	45.4	2061
30.5	116	71.3	5098
31.0	190	144.7	20938

APPENDIX B: MATERIALS AND METHODS

A. Demagnifier setup

The experimental data were acquired at the beamline P23 at PETRA III, DESY, Hamburg. The whole setup including the Bragg conditioner, sample, Bragg demagnifier, and detector was set up on a 2 m × 1 m large optical table. All crystals are composed of silicon (Si), have an asymmetry angle of $\alpha = \pm 5.92^\circ$ between the crystal surface normal and the crystallographic [110] direction, and dimensions of 21 cm × 8 cm × 2 cm. We used the Si (220) reflex. The nominal imaging parameters of the Bragg demagnifier crystals are given in Table I for energies between 29 and 31 keV. Each crystal was mounted on a high-precision hexapod [Physik Instrumente (PI) GmbH & Co. KG, Karlsruhe, Germany]. The detector was placed at a distance of $z_{2,y} = 0.90\,\mathrm{m}$ from the first crystal and $z_{2,x} = 0.57\,\mathrm{m}$ from the second crystal. For acquiring images with the Bragg demagnifier, we employed a high-resolution indirect detector system with a 24 µm thick LSO:Tb scintillator, a diffraction-limited optical microscope (Optique Peter, Lentilly, France) with a 5× objective lens with a numerical aperture of 0.14 (model 378-802-6, Mitutoyo Deutschland GmbH, Neuss, Germany), a 180 mm tubus lens resulting in 4.5× total optical magnification [79], and a pco.edge 5.5 CMOS camera (PCO AG, Kelheim, Germany) with an exposure time of 67 ms and a physical pixel size of 6.5 µm, yielding an effective pixel size of 1.44 µm in the image plane. Combined with the demagnification factor of $M = 25.7$ at 29 keV, the pixel size amounts to 37 µm in the object plane.

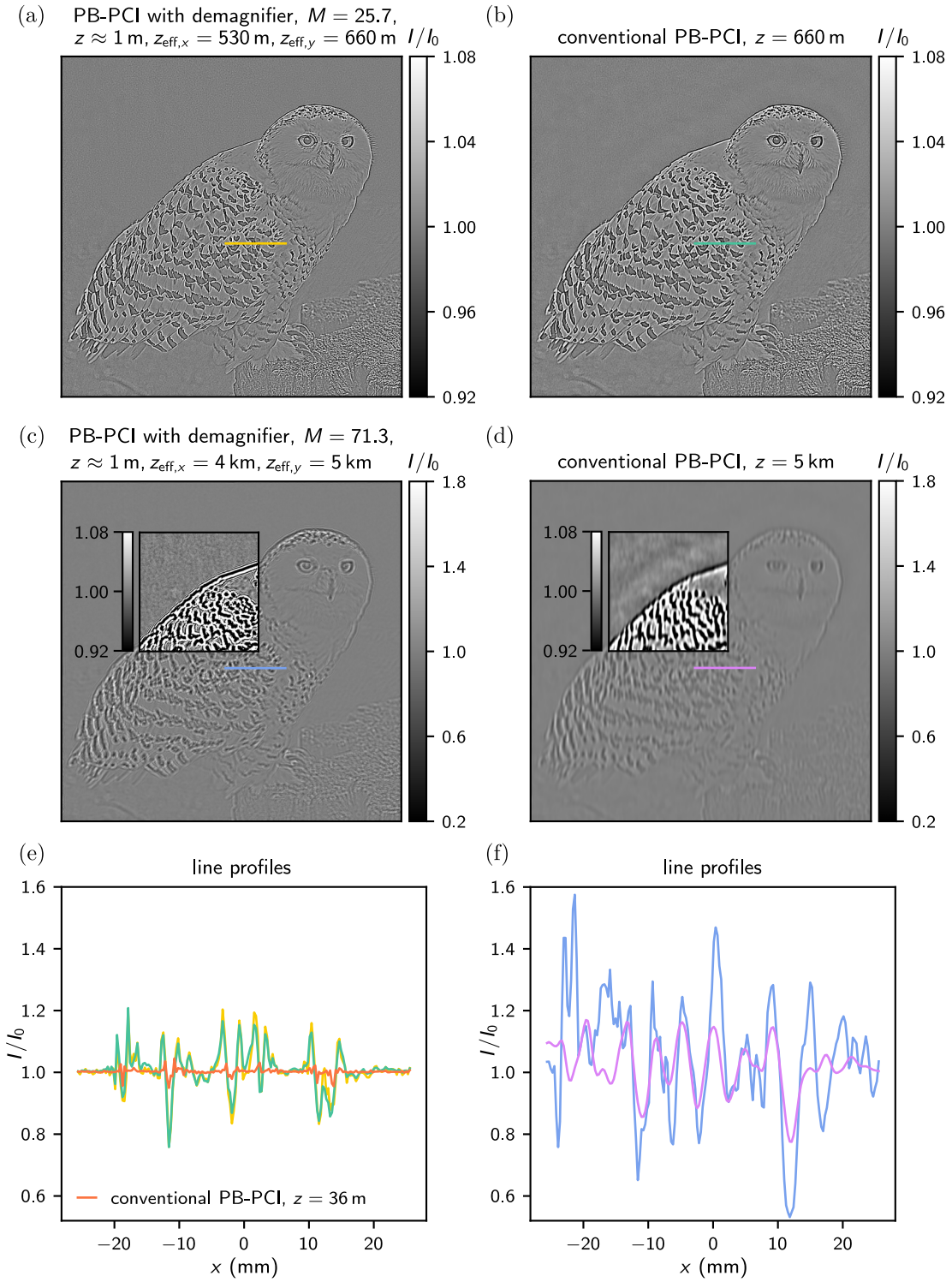


FIG. 6. Simulations as shown in Fig. 5, but for the source parameters of BM18 (ESRF-EBS) as stated in the literature [40] (see text). Simulations are shown for the Bragg demagnifier with a demagnification factor of (a) $M = 25.7$ and (c) $M = 71.3$ and physical distances of $z_x = 0.8\,\mathrm{m}$, $z_y = 1\,\mathrm{m}$ after demagnification. Simulations for conventional PB-PCI are shown at hypothetical physical propagation distances of (b) $z = 660\,\mathrm{m}$ and (d) $z = 5\,\mathrm{km}$. Note the difference in the color scale by a factor of 10 in panels (c) and (d). (e) Intensity line profiles as marked in panels (a) and (b) as well as conventional PB-PCI at 36 m [orange, image not shown since it is very similar to Fig. 5(b)]. (f) Intensity line profiles as marked in panels (c) and (d). Note, to allow for a better comparison, the images have been normalized to the average image intensity.

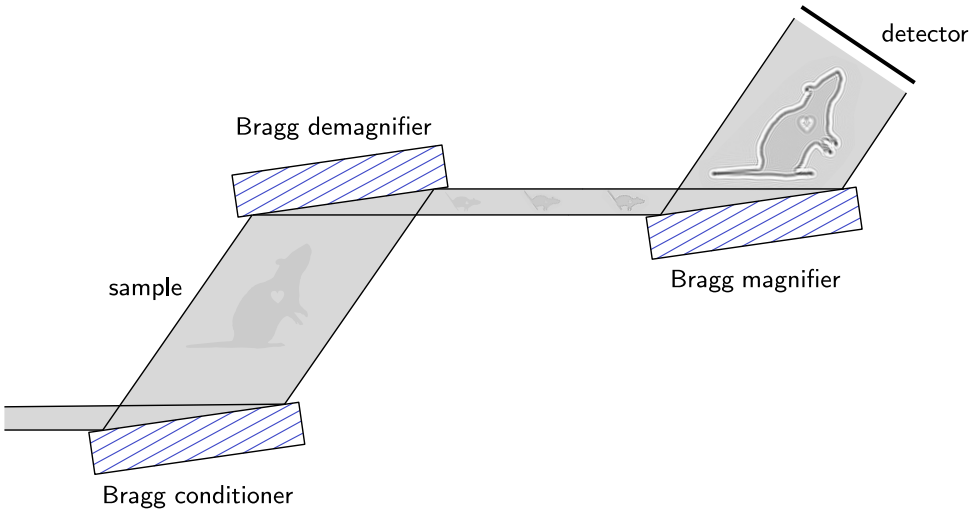


FIG. 7. Schematic of the combination Bragg conditioner, Bragg demagnifier, and Bragg magnifier in 1D. The Bragg magnifier allows the usage of an efficient large-area detector. Furthermore, when using the same type of crystals, the Bragg magnifier compensates the shift variance of the demagnifier; see text.

With the current proof-of-principle setup, stripe patterns occurred as artifacts in several images; see, e.g., the images of the liver lobe and the salamander (Fig. 3). The limited crystal polishing quality leads to structures in the flat field (empty beam), which could only be partly corrected due to drifts caused by the limited mechanical stability of the demonstrator setup compared to the very small incident angular acceptance of the demagnifier crystals ($\lesssim$1 µrad). With a dedicated setup similar to our proof-of-principle setup, but with an accordingly high mechanical stability in the 0.1 µrad range, the proposed technique can also achieve even higher demagnifications of up to about $M = 150$, which would allow for even longer effective propagation distances of up to $z_{\text{eff}} \approx 20$ km (see also Table I). With such a dedicated setup, routine applications such as PB-PCI tomography will also become feasible.

B. Conventional setup

For the conventional PB-PCI acquisitions, a Shad-o-Box 1K HS (Teledyne Dalsa, Waterloo, Canada) was placed 1 m downstream of the sample. To prevent saturation of the camera, we had to attenuate the beam by a factor of ∼250. The images were acquired with 67 ms exposure time and averaged over 20 acquisitions, resulting in a detected x-ray photon statistics of ∼15 000, which allows resolving the slight absorption contrast in Figs. 3(a) and 3(c) (right column). For the demagnifier setup, the detected x-ray statistics in the presented single acquisitions are comparable due to the reduced detection efficiency of the high-resolution indirect detector system [42]. For data acquisition and motor control, we used the control system *Concert* [80].

C. Samples

The tiger salamander (*Ambystoma tigrinum*) imaged in the experiment was a museum specimen from the Stuttgart State Museum of Natural History. The mouse liver was obtained from The Jackson Laboratory, USA. Both specimens were fixed in paraformaldehyde and stored in 70% ethanol.

APPENDIX C: SHIFT (IN)VARIANCE

In a shift-invariant imaging system, a translation of the object yields the same image, besides a displacement. In contrast, Bragg crystal optics are in general shift-variant imaging systems [81,82]. Due to asymmetric reflection, a lateral translation of the wave field leads to different propagation distances, which is a complication for phase retrieval [83,84]. For coplanar diffraction of a plane wave on a crystal surface, the relation between the incident and outgoing spatial frequencies k_{in} and k_{out} is given by [73]

$$k_{\text{out}} = k_0 \sin\left(\beta_{\text{out}} - \arccos\left[\cos\left(\beta_{\text{in}} - \arcsin\frac{k_{\text{in}}}{k_0}\right) + \cos\beta_{\text{out}} - \cos\beta_{\text{in}}\right]\right),$$

where β_{in} and β_{out} are the angles between the crystal surface and the incident or outgoing optical axis, respectively. These angles can be computed from dynamical diffraction theory [54]. As mentioned in the main text, the shift invariance of the demagnifier can be restored by adding a matched Bragg magnifier downstream (see Fig. 7). This can be best understood in Fourier space. A plane wave with spatial frequency $\mathbf{k}_{\text{in}}$ incident on the demagnifier results in a plane wave with the same spatial frequency $\mathbf{k}_{\text{out}} = \mathbf{k}_{\text{in}}$ in the detector plane behind the magnifier. Only the phase and amplitude are altered by the crystals and the free space propagation. Consequently, the modulation of the propagated wave field can be described by a transfer function; i.e., the propagated wave field is given by a convolution of the incident wave field with a coherent point-spread function.

[1] T. Salditt, T. Aspelmeier, and S. Aeffner, *Biomedical Imaging* (De Gruyter, Berlin, Germany, 2017), p. 244

[2] M. Endrizzi, X-ray phase-contrast imaging, Nucl. Instrum. Methods Phys. Res., Sect. A **878**, 88 (2018).

[3] H. N. Chapman and K. A. Nugent, Coherent lensless x-ray imaging, Nat. Photonics **4**, 833 (2010).

[4] F. Pfeiffer, J. Herzen, M. Willner, M. Chabior, S. Auweter, M. Reiser, and F. Bamberg, Grating-based x-ray phase contrast for biomedical imaging applications, Z. Med. Phys. **23**, 176 (2013).

[5] V. V. Lider and M. V. Kovalchuk, X-ray phase-contrast methods, Crystallogr. Rep. **58**, 769 (2013).

[6] S. Lang, I. Zanette, M. Dominietto, M. Langer, A. Rack, G. Schulz, G. Le Duc, C. David, J. Mohr, F. Pfeiffer, B. Müller, and T. Weitkamp, Experimental comparison of grating- and propagation-based hard x-ray phase tomography of soft tissue, J. Appl. Phys. **116**, 154903 (2014).

[7] S. Tao, C. He, X. Hao, C. Kuang, and X. Liu, Principles of different x-ray phase-contrast imaging: A review, Appl. Sci. **11**, 2971 (2021).

[8] S. C. Mayo, A. W. Stevenson, and S. W. Wilkins, In-line phase-contrast x-ray imaging and tomography for materials science, Materials **5**, 937 (2012).

[9] M. Cotte, P.-O. Autran, C. Berruyer, C. Dejoie, J. Susini, and P. Tafforeau, Cultural and natural heritage at the ESRF: Looking back and to the future, Synchrotron Radiat. News **32**, 34 (2019).

[10] O. Betz, U. Wegst, D. Weide, M. Heethoff, L. Helfen, W.-K. Lee, and P. Cloetens, Imaging applications of synchrotron x-ray phase-contrast microtomography in biological morphology and biomaterials science. I. General aspects of the technique and its advantages in the analysis of millimetre-sized arthropod structure, J. Microsc. **227**, 51 (2007).

[11] J. Moosmann, A. Ershov, V. Altapova, T. Baumbach, M. S. Prasad, C. LaBonne, X. Xiao, J. Kashef, and R. Hofmann, X-ray phase-contrast *in vivo* microtomography probes new aspects of *Xenopus* gastrulation, Nature (London) **497**, 374 (2013).

[12] R. A. Lewis, Medical phase contrast x-ray imaging: Current status and future prospects, Phys. Med. Biol. **49**, 3573 (2004).

[13] A. Bravin, P. Coan, and P. Suortti, X-ray phase-contrast imaging: From pre-clinical applications towards clinics, Phys. Med. Biol. **58**, R1 (2013).

[14] J. Kastner, C. Heinzl, B. Plank, D. Salaberger, C. Gusenbauer, and S. Senck, New x-ray computed tomography methods for research and industry, in *7th Conference on Industrial Computed Tomography (iCT2017)* (2017), Vol. 22.

[15] S. T. Taba, T. E. Gureyev, M. Alakhras, S. Lewis, D. Lockie, and P. C. Brennan, X-ray phase-contrast technology in breast imaging: Principles, options, and clinical application, Am. J. Roentgenol. **211**, 133 (2018).

[16] M. Eckermann, J. Frohn, M. Reichardt, M. Osterhoff, M. Sprung, F. Westermeier, A. Tzankov, C. Werlein, M. Kühnel, D. Jonigk, and T. Salditt, 3D virtual pathohistology of lung tissue from COVID-19 patients based on phase contrast x-ray tomography, eLife **9**, e60408 (2020).

[17] T. J. Davis, D. Gao, T. Gureyev, A. Stevenson, and S. Wilkins, Phase-contrast imaging of weakly absorbing materials using hard x-rays, Nature (London) **373**, 595 (1995).

[18] D. Chapman, W. Thomlinson, R. Johnston, D. Washburn, E. Pisano, N. Gmür, Z. Zhong, R. Menk, F. Arfelli, and D. Sayers, Diffraction enhanced x-ray imaging, Phys. Med. Biol. **42**, 2015 (1997).

[19] C. David, B. Nöhammer, H. H. Solak, and E. Ziegler, Differential x-ray phase contrast imaging using a shearing interferometer, Appl. Phys. Lett. **81**, 3287 (2002).

[20] A. Momose, S. Kawamoto, I. Koyama, Y. Hamaishi, K. Takai, and Y. Suzuki, Demonstration of x-ray Talbot interferometry, Jpn. J. Appl. Phys. **42**, L866 (2003).

[21] K. S. Morgan, D. M. Paganin, and K. K. W. Siu, X-ray phase imaging with a paper analyzer, Appl. Phys. Lett. **100**, 124102 (2012).

[22] M.-C. Zdora, State of the art of x-ray speckle-based phase-contrast and dark-field imaging, J. Imaging **4**, 60 (2018).

[23] A. Snigirev, I. Snigireva, V. Kohn, S. Kuznetsov, and I. Schelokov, On the possibilities of x-ray phase contrast microimaging by coherent high-energy synchrotron radiation, Rev. Sci. Instrum. **66**, 5486 (1995).

[24] S. W. Wilkins, T. E. Gureyev, D. Gao, A. Pogany, and A. W. Stevenson, Phase-contrast imaging using polychromatic hard x-rays, Nature (London) **384**, 335 (1996).

[25] P. Cloetens, W. Ludwig, J. Baruchel, D. Van Dyck, J. Van Landuyt, J. Guigay, and M. Schlenker, Holotomography: Quantitative phase tomography with micrometer resolution using hard synchrotron radiation X rays, Appl. Phys. Lett. **75**, 2912 (1999).

[26] A. Zamir, O. J. Arthurs, C. K. Hagen, P. C. Diemoz, T. Brochard, A. Bravin, N. J. Sebire, and A. Olivo, X-ray phase contrast tomography; proof of principle for post-mortem imaging, Br. J. Radiol. **89**, 20150565 (2016).

[27] W. L. Wagner, F. Wuennemann, S. Pacilé, J. Albers, F. Arfelli, D. Dreossi, J. Biederer, P. Konietzke, W. Stiller, M. O. Wielpütz *et al.*, Towards synchrotron phase-contrast lung imaging in patients—A proof-of-concept study on porcine lungs in a human-scale chest phantom, J. Synchrotron Radiat. **25**, 1827 (2018).

[28] M. Donnelley, K. S. Morgan, R. Gradl, M. Klein, D. Hausermann, C. Hall, A. Maksimenko, and D. W. Parsons, Live-pig-airway surface imaging and whole-pig CT at the Australian Synchrotron Imaging and Medical Beamline, J. Synchrotron Radiat. **26**, 175 (2019).

[29] G. E. Barbone, A. Bravin, A. Mittone, S. Grosu, J. Ricke, G. Cavaletti, V. Djonov, and P. Coan, High-spatial-resolution three-dimensional imaging of human spinal cord and column anatomy with postmortem x-ray phase-contrast micro-CT, Radiology (2020).

[30] C. Walsh, P. Tafforeau, W. Wagner, D. Jafree, A. Bellier, C. Werlein, M. Kühnel, E. Boller, S. Walker-Samuel, J. Robertus *et al.*, Imaging intact human organs with local resolution of cellular structures using hierarchical phase-contrast tomography, Nat. Methods **18**, 1532 (2021).

[31] P. Baran, S. Pacile, Y. I. Nesterets, S. C. Mayo, C. Dullin, D. Dreossi, F. Arfelli, D. Thompson, D. Lockie, M. McCormack *et al.*, Optimization of propagation-based x-ray phase-contrast tomography for breast cancer imaging, Phys. Med. Biol. **62**, 2315 (2017).

[32] L. Broche, P. Pisa, L. Porra, L. Degrugilliers, A. Bravin, M. Pellegrini, J. B. Borges, G. Perchiazzi, A. Larsson, G. Hedenstierna, and S. Bayat, Individual airway closure characterized *in vivo* by phase-contrast CT imaging in injured rabbit lung, Crit. Care Med. **47**, e774 (2019).

[33] C. Tavakoli, E. Cuccione, C. Dumot, D. Cormode, M. Wiart, H. Elleaume, and E. Brun, Tracking cells in the brain of small

animals using synchrotron multi-spectral phase contrast imaging, in *Medical Imaging 2021: Physics of Medical Imaging* (SPIE, Bellingham, Washington, USA, 2021), Vol. 11595, pp. 1218–1224.

[34] B. D. Arhatari, A. W. Stevenson, B. Abbey, Y. I. Nesterets, A. Maksimenko, C. J. Hall, D. Thompson, S. C. Mayo, T. Fiala, H. M. Quiney *et al.*, X-ray phase-contrast computed tomography for soft tissue imaging at the Imaging and Medical Beamline (IMBL) of the Australian Synchrotron, Appl. Sci. **11**, 4120 (2021).

[35] M. Cotte, K. Dollman, V. Fernandez, V. Gonzalez, F. Vanmeert, L. Monico, C. Dejoie, M. Burghammer, L. Huder, S. Fisher *et al.*, New opportunities offered by the ESRF to the cultural and natural heritage communities, Synchrotron Radiat. News **35**, 3 (2022).

[36] I. Häggmark, K. Shaker, S. Nyrén, B. Al-Amiry, E. Abadi, W. P. Segars, E. Samei, and H. M. Hertz, Phase-contrast virtual chest radiography, Proc. Natl. Acad. Sci. USA **120**, e2210214120 (2023).

[37] J. Albers, W. L. Wagner, M. O. Fiedler, A. Rothermel, F. Wünnemann, F. Di Lillo, D. Dreossi, N. Sodini, E. Baratella, M. Confalonieri, F. Arfelli, A. Kalenka, J. Lotz, J. Biederer, M. O. Wielpütz, H.-U. Kauczor, F. Alves, G. Tromba, and C. Dullin, High resolution propagation-based lung imaging at clinically relevant x-ray dose levels, Sci. Rep. **13**, 4788 (2023).

[38] I. Gunaseelan, A. Amin Zadeh, B. Arhatari, A. Maksimenko, C. Hall, D. Hausermann, B. Kumar, J. Fox, H. Quiney, D. Lockie, S. Lewis, P. Brennan, T. Gureyev, and S. Tavakoli Taba, Propagation-based phase-contrast imaging of the breast: Image quality and the effect of x-ray energy and radiation dose, Br. J. Radiol. **96**, 20221189 (2023).

[39] F. Cianciosi, A.-L. Buisson, P. Tafforeau, and P. Van Vaerenbergh, BM18, the new ESRF-EBS beamline for hierarchical phase-contrast tomography, in *Proc. MEDSI'20*, Chicago, IL, USA (JACOW Publishing, Geneva, Switzerland, 2021), pp. 1–5.

[40] T. Lang, N. Saeidnezhad, K. Dremel, D. Weller, M. Diez, A. M. Stock, T. Sauer, F. Cianciosi, C. Jarnias, P. Tafforeau, and S. Zabler, Multiscale phase-contrast tomography at BM18, e-J. Nondestr. Test. **28** (2023).

[41] J. M. Cowley, Electron microdiffraction, in *Advances in Electronics and Electron Physics*, edited by L. Marton (Academic Press, Cambridge, MA, 1978), Vol. 46, pp. 1–53.

[42] R. Spiecker, P. Pfeiffer, A. Biswal, M. Shcherbinin, M. Spiecker, H. Hessdorfer, M. Hurst, Y. Zharov, V. Bellucci, T. Farago *et al.*, Dose-efficient *in vivo* x-ray phase contrast imaging at micrometer resolution, Optica **10**, 1633 (2023).

[43] S. Si-Mohamed, S. Boccalini, P.-A. Rodesch, R. Dessouky, E. Lahoud, T. Broussaud, M. Sigovan, D. Gamondes, P. Coulon, Y. Yagil, L. Boussel, and P. Douek, Feasibility of lung imaging with a large field-of-view spectral photon-counting CT system, Diagn. Interventional Imaging **102**, 305 (2021).

[44] W. J. Boettinger, H. E. Burdette, and M. Kuriyama, X-ray magnifier, Rev. Sci. Instrum. **50**, 26 (1979).

[45] K. Kobayashi, K. Izumi, H. Kimura, S. Kimura, T. Ibuki, Y. Yokoyama, Y. Tsusaka, Y. Kagoshima, and J. Matsui, X-ray phase-contrast imaging with submicron resolution by using extremely asymmetric Bragg diffractions, Appl. Phys. Lett. **78**, 132 (2001).

[46] R. D. Spal, Submicrometer resolution hard x-ray holography with the asymmetric Bragg diffraction microscope, Phys. Rev. Lett. **86**, 3044 (2001).

[47] M. Stampanoni, G. Borchert, R. Abela, and P. Rüegsegger, Bragg magnifier: A detector for submicrometer x-ray computer tomography, J. Appl. Phys. **92**, 7630 (2002).

[48] P. Modregger, D. Lübbert, P. Schäfer, and R. Köhler, Magnified x-ray phase imaging using asymmetric Bragg reflection: Experiment and theory, Phys. Rev. B **74**, 054107 (2006).

[49] P. Vagovič, D. Korytár, P. Mikulík, A. Cecilia, C. Ferrari, Y. Yang, D. Hänschke, E. Hamann, D. Pelliccia, T. A. Lafford, M. Fiederle, and T. Baumbach, In-line Bragg magnifier based on V-shaped germanium crystals, J. Synchrotron Radiat. **18**, 753 (2011).

[50] K. Hirano, Y. Takahashi, and H. Sugiyama, Development and application of variable-magnification x-ray Bragg magnifiers, Nucl. Instrum. Methods Phys. Res., Sect. A **741**, 78 (2014).

[51] N. Watanabe, M. Suzuki, Y. Higashi, and N. Sakabe, Rotated-inclined focusing monochromator with simultaneous tuning of asymmetry factor and radius of curvature over a wide wavelength range, J. Synchrotron Radiat. **6**, 64 (1999).

[52] Y. Tsusaka, K. Yokoyama, S. Takeda, M. Urakawa, Y. Kagoshima, J. Matsui, S. Kimura, H. Kimura, K. Kobayashi, and K. Izumi, Formation of parallel x-ray microbeam and its application, Jpn. J. Appl. Phys. **39**, L635 (2000).

[53] K. Hirano and Y. Takahashi, Applications of x-ray magnifier and demagnifier to angle-resolved x-ray computed tomography, J. Phys.: Conf. Ser. **425**, 192004 (2013).

[54] A. Authier, *Dynamical Theory of X-ray Diffraction* (Oxford University Press Inc., New York, 2004), Vol. 11, p. 189.

[55] E. Abbe, Beiträge zur Theorie des Mikroskops und der mikroskopischen Wahrnehmung, Archiv. Mikroskopische Anatomie **9**, 413 (1873).

[56] M. Martinson, N. Samadi, B. Bassey, A. Gomez, and D. Chapman, Phase-preserving beam expander for biomedical x-ray imaging, J. Synchrotron Radiat. **22**, 801 (2015).

[57] O. Márkus, I. Greving, E. Kornemann, M. Storm, F. Beckmann, J. Mohr, and A. Last, Optimizing illumination for full field imaging at high brilliance hard x-ray synchrotron sources, Opt. Express **26**, 30435 (2018).

[58] C. Reinhard, M. Drakopoulos, S. I. Ahmed, H. Deyhle, A. James, C. M. Charlesworth, M. Burt, J. Sutter, S. Alexander, P. Garland *et al.*, Beamline K11 DIAD: A new instrument for dual imaging and diffraction at diamond light source, J. Synchrotron Radiat. **28**, 1985 (2021).

[59] T. Matsushita and H. Hashizume, *Handbook on Synchrotron Radiation*, edited by E. Koch (North Holland Publishing Company, Amsterdam, Netherlands, 1983), Vol. 1, Chap. 4.

[60] F. E. Christensen, A. Hornstrup, P. K. Frederiksen, S. Abdali, P. Grundsoe, H. W. Schnopper, R. A. Lewis, C. J. Hall, and K. N. Borozdin, Expanded beam x-ray optics calibration facility at the Daresbury Synchrotron, in *Multilayer and Grazing Incidence X-ray/EUV Optics II* (SPIE, Bellingham, Washington, 1994), Vol. 2011, pp. 540–548.

[61] C. Kamezawa, K. Hyodo, C. Tokunaga, T. Tsukada, and S. Matushita, Large-view x-ray imaging for medical applications using the world's only vertically polarized synchrotron radiation beam and a single asymmetric Si crystal, Phys. Med. Biol. **68**, 195010 (2023).

[62] T. J. Davis, T. E. Gureyev, D. Gao, A. W. Stevenson, and S. W. Wilkins, X-ray image contrast from a simple phase object, Phys. Rev. Lett. **74**, 3173 (1995).

[63] S. D. Shastri, Combining flat crystals, bent crystals and compound refractive lenses for high-energy x-ray optics, J. Synchrotron Radiat. **11**, 150 (2004).

[64] A. Bravin, Exploiting the x-ray refraction contrast with an analyser: The state of the art, J. Phys. D **36**, A24 (2003).

[65] F. Lenz and W. Scheffels, Das Zusammenwirken von Phasen- und Amplitudenkontrast in der elektronenmikroskopischen Abbildung, Z. Naturforsch. A **13**, 226 (1958).

[66] E. J. Kirkland, Some image approximations, in *Advanced Computing in Electron Microscopy* (Springer, Cham, Switzerland, 2020), pp. 37–80.

[67] A. Momose and J. Fukuda, Phase-contrast radiographs of nonstained rat cerebellar specimen, Med. Phys. **22**, 375 (1995).

[68] F. Thon, Zur Defokussierungsabhängigkeit des Phasenkontrastes bei der elektronenmikroskopischen Abbildung, Z. Naturforsch. A **21**, 476 (1966).

[69] A. J. Morgan, K. T. Murray, M. Prasciolu, H. Fleckenstein, O. Yefanov, P. Villanueva-Perez, V. Mariani, M. Domaracky, M. Kuhn, S. Aplin, I. Mohacsi, M. Messerschmidt, K. Stachnik, Y. Du, A. Burkhart, A. Meents, E. Nazaretski, H. Yan, X. Huang, Y. S. Chu *et al.*, Ptychographic x-ray speckle tracking with multi-layer Laue lens systems, J. Appl. Crystallogr. **53**, 927 (2020).

[70] A. Rohou and N. Grigorieff, CTFFIND4: Fast and accurate defocus estimation from electron micrographs, J. Struct. Biol. **192**, 216 (2015).

[71] R. Pretzsch, M. Dries, S. Hettler, M. Spiecker, M. Obermair, and D. Gerthsen, Investigation of hole-free phase plate performance in transmission electron microscopy under different operation conditions by experiments and simulations, Adv. Struct. Chem. Imaging **5**, 5 (2019).

[72] X. Huang, A. Macrander, M. Honnicke, Y. Cai, and P. Fernandez, Dispersive spread of virtual sources by asymmetric x-ray monochromators, J. Appl. Crystallogr. **45**, 255 (2012).

[73] R. Spiecker, Bragg magnifier optics for dose-efficient x-ray phase contrast imaging, Dissertation, Karlsruhe Institute of Technology, 2024, doi: 10.5445/IR/1000162889.

[74] Z. Huang and R. D. Ruth, Laser-electron storage ring, Phys. Rev. Lett. **80**, 976 (1998).

[75] M. Bech, O. Bunk, C. David, R. Ruth, J. Rifkin, R. Loewen, R. Feidenhans'l, and F. Pfeiffer, Hard x-ray phase-contrast imaging with the compact light source based on inverse Compton x-rays, J. Synchrotron Radiat. **16**, 43 (2009).

[76] B. Günther, R. Gradl, C. Jud, E. Eggl, J. Huang, S. Kulpe, K. Achterhold, B. Gleich, M. Dierolf, and F. Pfeiffer, The versatile x-ray beamline of the Munich Compact Light Source: Design, instrumentation and applications, J. Synchrotron Radiat. **27**, 1395 (2020).

[77] B. Hornberger, J. Kasahara, R. Ruth, R. Loewen, and J. Khaydarov, Inverse Compton scattering x-ray source for research, industry and medical applications, in *International Conference on X-ray Lasers 2020* (SPIE, Bellingham, Washington, 2021), Vol. 11886, pp. 51–60.

[78] C. G. Schroer, H.-C. Wille, O. H. Seeck, K. Bagschik, H. Schulte-Schrepping, M. Tischer, H. Graafsma, W. Laasch, K. Baev, S. Klumpp, R. Bartolini, H. Reichert, W. Leemans, and E. Weckert, The synchrotron radiation source PETRA III and its future ultra-low-emittance upgrade PETRA IV, Eur. Phys. J. Plus **137**, 1312 (2022).

[79] P.-A. Douissard, A. Cecilia, X. Rochet, X. Chapel, T. Martin, T. van de Kamp, L. Helfen, T. Baumbach, L. Luquot, X. Xiao *et al.*, A versatile indirect detector design for hard x-ray microimaging, J. Instrum. **7**, P09016 (2012).

[80] M. Vogelgesang, T. Farago, T. F. Morgeneyer, L. Helfen, T. dos Santos Rolo, A. Myagotin, and T. Baumbach, Real-time image-content-based beamline control for smart 4D x-ray imaging, J. Synchrotron Radiat. **23**, 1254 (2016).

[81] P. Modregger, D. Lübbert, P. Schäfer, R. Köhler, T. Weitkamp, M. Hanke, and T. Baumbach, Fresnel diffraction in the case of an inclined image plane, Opt. Express **16**, 5141 (2008).

[82] S. Hrivňak, J. Uličný, and P. Vagovič, Fast fresnel propagation through a set of inclined reflecting planes applicable for x-ray imaging, Opt. Express **26**, 34569 (2018).

[83] P. Vagovič, L. Švéda, A. Cecilia, E. Hamann, D. Pelliccia, E. Gimenez, D. Korytár, K. M. Pavlov, Z. Zápražný, M. Zuber *et al.*, X-ray Bragg magnifier microscope as a linear shift invariant imaging system: Image formation and phase retrieval, Opt. Express **22**, 21508 (2014).

[84] S. Hrivňak, J. Uličný, L. Mikeš, A. Cecilia, E. Hamann, T. Baumbach, L. Švéda, Z. Zápražný, D. Korytár, E. Gimenez-Navarro *et al.*, Single-distance phase retrieval algorithm for Bragg magnifier microscope, Opt. Express **24**, 27753 (2016).